


Jingzhu Wang  · Akihisa Abe · Shigeru Nishio · Yiwei Wang · Chenguang Huang

# Sequential observation of rebound shock wave generated by collapse of vapor bubble in BOS system

Received: 13 November 2017 / Revised: 24 February 2018 / Accepted: 6 March 2018  
© The Visualization Society of Japan 2018

**Abstract** The paper reports on a pressure measurement of underwater shock waves generated by collapse of a vapor bubble using the background-oriented schlieren (BOS) technique. In the BOS system, the vapor bubble is induced by an underwater electric discharge. To estimate background-element displacement induced by the underwater shock wave, a spatiotemporal derivative (STD) algorithm is applied in image processing. Furthermore, the accuracy of the STD algorithm is evaluated using the images obtained with our BOS system relative to the cross-correlation method. Subsequently, the pressure distributions are obtained by solving the Poisson equation and applying a filtered-back projection algorithm. An experiment to visualize the behaviors of the underwater shock waves is also carried out using the shadowgraph method. As a result, the pressure waveforms estimated by the BOS technique keep consistent with that in experimental profiles. The pressure attenuations behind the underwater shock wave are also in good agreements with the experimental measurements. It is expected that the BOS technique will probably overcome the problems associated with the conventional method of pressure measurement related to the collapse of microbubbles, and becomes a promising means of quantitatively measuring high-speed phenomena.

**Keywords** Pressure measurement · Underwater shock wave · Collapse of vapor bubble · High-voltage-power supply · BOS technique · STD algorithm

## 1 Introduction

The concept of the background-oriented schlieren (BOS) was first proposed as a further simplification of the optical schlieren system patented by Meier (1999). The feasibility of the BOS technique was demonstrated by Raffel et al. (2000) and Richard et al. (2001). Raffel et al. (2000) built a BOS system to visualize a full-scale helicopter in flight and investigated the effects of the Reynolds number on vortex developments from the blade tips. They reported that the investigation could be carried out more easily when using the BOS technique, relative to the laser-based techniques. The vortex shedding on a cylinder in a transonic wind

---

J. Wang (✉) · Y. Wang · C. Huang  
Key Laboratory for Mechanics in Fluid Solid Coupling Systems, Institute of Mechanics, Chinese Academy of Sciences,  
No.15 Beisihuangxi Road, Haidian District, Beijing 100190, China  
E-mail: wangjingzhu@imech.ac.cn  
Tel.: +861082544291

J. Wang · Y. Wang · C. Huang  
School of Engineering Science, University of Chinese Academy of Sciences, Beijing 100049, China

A. Abe · S. Nishio  
Graduate School of Maritime Sciences, Kobe University, 5-1-1 Fukaeminami-machi, Higashinada-ku, Kobe, Hyogo 658-0022, Japan

Published online: 20 April 2018

tunnel was also analyzed in detail using the BOS techniques by Richard et al. (2001). To enhance the applicability of the BOS technique, Meier (2002) extended two other types, namely, background-oriented stereoscopic schlieren (BOSS) and background-oriented optical tomography (BOOT) based on the BOS technique. The former is achieved using two cameras that are synchronized to capture two pairs of images from different viewing angles, after which spatial location of the identifiable phase is evaluated for unsteady objects. The latter is similar to other tomographic techniques, in that it enables the three-dimensional reconstruction of unidentifiable objects. Venkatakrisnan and Meier (2004) carried out an experiment of an axisymmetric supersonic flow over a cone-cylinder model and first verified the density field obtained with the BOS technique by comparing cone tables and isentropic solution. The results underlined the fact that the BOS technique can enable the quantitative visualization of density field in a flow. Compared to the shadowgraph, schlieren photograph, or interferometry, the BOS technique requires only a small amount of optical equipment, combined with computer techniques, to produce visualization both quantitatively and precisely. In recent years, the BOS technique has been evolved as an attractive option for quantitative visualization of the flow. Kindler et al. (2007) applied the BOSS technique to the investigation of blade tip vortexes in full-scale helicopter flight tests and first reported a reconstruction of the compressible vortex. The BOOT technique was also used by Venkatakrisnan and Suriyanarayanan (2009) to obtain a three-dimensional density field in a supersonic shock-separated flow. They carried out a reconstruction using 19 non-simultaneous images, thus yielding a mean density field. Based on this work, they also reconstructed three-dimensional density field of the blast wave generated by a micro-explosion (Venkatakrisnan et al. 2013). These results clearly prove the ability of the BOS technique to visualize and quantify complex density flow. Yamamoto et al. (2015) applied the BOS technique to the visualization of a laser-induced underwater shock wave for the first time and obtained the displacement field using a conventional cross-correlation method. The maximum displacement was about 1 pixel in their BOS system. Based on their work, Hayasaka et al. (2016) reconstructed the displacement field using a tomographic method and attained the pressure profile.

The principle of the BOS technique is on the basis of the variations in refractive index caused by density gradients resulting in the distortion in images. By the contrast between an undistorted and distorted image, background-element displacements are determined and then used to obtain the required parameters such as density or pressure. For estimating the background-element displacements, the cross-correlation methods based on a fast fourier transform (FFT) and FFT with window deformation (FFT-wd) algorithm commonly used in particle image velocimetry technique are employed (Venkatakrisnan and Meier 2004; Venkatakrisnan and Suriyanarayanan 2009; Yamamoto et al. 2015). However, an underwater shock front with a density jump and small radii of curvature probably induce not only displacements in the background but also deformation. This could exacerbate the difficulties facing in the accurate detection of the background-element displacements using both of the algorithms. Consequently, an accurate estimate of sub-pixel displacement is required for application of the BOS technique to measure the pressure of an underwater shock wave. It is well known that the spatiotemporal derivative (STD) algorithm provides an excellent estimation of a sub-pixel displacement and has also been applied to the flow field (Nishio et al. 1998) and wall shear stress measurements (Okuno 1995). Sugii et al. (2000) also pointed out that sub-pixel displacement could be accurately evaluated using the STD algorithm. Hayasaka et al. (2016) obtained a spatial resolution of per pixel and a better accuracy using an optical flow method based on Liu and Shen (2008).

In the present study, we try to use the BOS technique to visualize and quantify the pressures of rebound shock wave generated from collapse of a vapor bubble as a result of an underwater electric discharge. In the imaging process, we use the STD algorithm based on the study by Sugii et al. (2000), and then evaluate on its accuracy by comparing with the FFT and the FFT-wd algorithms. The Poisson equation is solved using the central differential method in terms of these background-element displacements. The distribution of refractive index is acquired by employing the filtered-back projection (FBP) algorithm with a Shepp–Logan filter to reconstruct the projections obtained with the Poisson equation. Next, the pressures behind the underwater shock waves are attained using the state equations for water. The shadowgraph observation is carried out to grasp on the generation state of the underwater shock waves. Finally, the pressure waveforms and attenuations of the underwater shock waves predicted by the BOS technique are compared with the experimental measurements to verify the pressure qualification of the BOS technique.

## 2 Experimental setup for BOS system

Figure 1 shows a schematic of the experimental setup for the BOS system. The system consisted of a background covered with random dots, a high-speed camera (MEMRECAM HX-3, Nac Image Technology), and a metal halide lamp as back illumination (LS-M350, SUMITA optical glass Inc.). A high-voltage-power supply (HPS 18K-A, Tamaoki Electronics Co., Ltd.) was used to trigger underwater electric discharges in a water tank. The dimensions of the water tank were 255 mm (L)  $\times$  180 mm (W)  $\times$  180 mm (H). Given the mechanism of underwater electric discharge, first shock waves are generated by the expansion of the thermal plasma channel consisting of high-temperature vapor. A vapor bubble is induced at the tips of the two electrodes. Next, with the collapse of the vapor bubble, rebound shock waves are produced. The electrodes were tungsten and the spark gap of the electrodes was 4 mm. The output power of the power supply was 49.8 kV. In addition, the size per pixel of the CMOS sensor of the camera was about 18  $\mu\text{m}$  in the system.

Based on the results of a study by Venkatakrishnan and Meier (2004), the background-element displacement of  $x$  component and  $y$  component at the screen plane of the camera,  $\Delta x$  and  $\Delta y$ , are presented as follows,

$$\Delta x = \frac{Z_D f}{Z_B} \frac{1}{n_0} \int_{Z_D - \Delta Z_D}^{Z_D + \Delta Z_D} \frac{\partial n}{\partial x} dz, \quad (1)$$

$$\Delta y = \frac{Z_D f}{Z_B} \frac{1}{n_0} \int_{Z_D - \Delta Z_D}^{Z_D + \Delta Z_D} \frac{\partial n}{\partial y} dz, \quad (2)$$

where  $z$  axis is the direction of the optical path,  $Z_D$  is the distance from the background to the discharge point and  $\Delta Z_D$  is the half-width of the region of the density gradient,  $\Delta Z_D \ll Z_D$ .  $n$  is the refractive index, and  $f$  is the focal distance of the lens.  $n_0$  is 1.333 at 15  $^\circ\text{C}$  under the atmospheric pressure. The distances  $Z_B$  and  $Z_D$  were 1760 mm and 500 mm, respectively, in our BOS system.

## 3 Image processing

### 3.1 Spatiotemporal derivative (STD) algorithm

Sugii et al. (2000) applied the least squares method within an interrogation window to solve the governing equation of the STD algorithm proposed by Horn and Schunck (1981). The background-element displacements are, therefore, obtained using the following equation assuming  $\Delta x$  and  $\Delta y$  to be constant within an interrogation window.

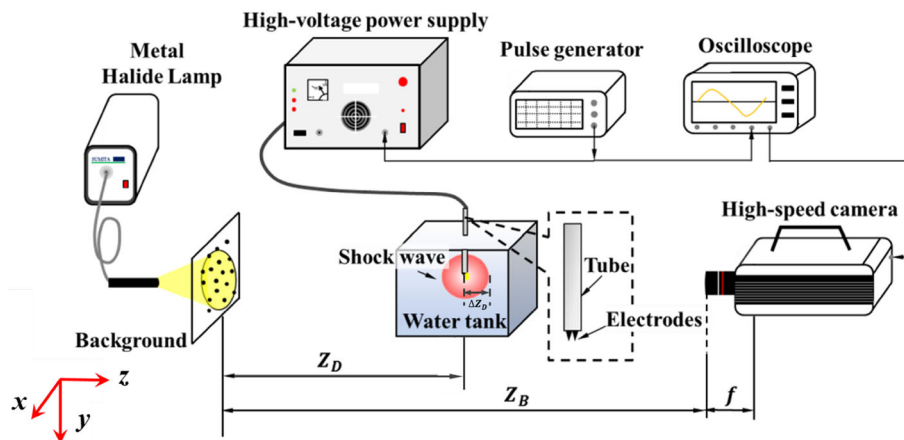


Fig. 1 Schematic of experimental setup for BOS system

$$\begin{pmatrix} \sum (f_{ijk})_x^2 & \sum (f_{ijk})_y (f_{ijk})_x \\ \sum (f_{ijk})_y (f_{ijk})_x & \sum (f_{ijk})_y^2 \end{pmatrix} \begin{pmatrix} \Delta x / \Delta t \\ \Delta y / \Delta t \end{pmatrix} = \begin{pmatrix} -\sum (f_{ijk})_x (f_{ijk})_t \\ -\sum (f_{ijk})_y (f_{ijk})_t \end{pmatrix}, \quad (3)$$

where  $f_{ijk}$  is the image brightness at the intersection of the  $i$  th row and  $j$  th column in the  $k$  th image frame.  $(f_{ijk})_x$ ,  $(f_{ijk})_y$ , and  $(f_{ijk})_t$  are the partial derivatives of the image brightness with  $x$ ,  $y$ , and  $t$ , respectively. In the analysis,  $\Delta t$  was suggested to be 1 considering the application of the STD algorithm to the imaging processing in the BOS method.

To develop a high sub-pixel accuracy, it is necessary for all the  $(f_{ijk})_x$ ,  $(f_{ijk})_y$ ,  $(f_{ijk})_t$  estimates to refer to the same point at the same time. In the study by Sugii et al. (2000), a cube formed by the eight brightness values, as shown in Fig. 2, was introduced to achieve this purpose. The black points at the corners of the cube are the brightness values obtained from the undistorted and distorted images, respectively. The red point at the central point of the cube is the position at which partial derivatives are calculated using the eight brightness values at the corners. The estimates of  $(f_{ijk})_x$ ,  $(f_{ijk})_y$ ,  $(f_{ijk})_t$  are as follows.

$$(f_{ijk})_t = \sum_i^{i+1} \sum_j^{j+1} (f_{ijk+1} - f_{ijk}) / 4\Delta t, \quad (f_{ijk})_x = \sum_j^{j+1} \sum_k^{k+1} (f_{i+1jk} - f_{ijk}) / 4\Delta x, \quad (f_{ijk})_y = \sum_i^{i+1} \sum_k^{k+1} (f_{ij+1k} - f_{ijk}) / 4\Delta y \quad (4)$$

### 3.2 Evaluation of the accuracy

The FFT and FFT-wd algorithms were also introduced to estimate the background-element displacements. In the present study, an open-source toolbox of the *PIVlab* provided by Thielicke (2014) was used to execute the codes of the FFT and FFT-wd algorithms. The  $2 \times 3$ -point sub-pixel estimator was used in the two algorithms through the *PIVlab* in MATLAB. Taking a  $4 \times 4$ -pixel interrogation window as an example, Table 1 shows the STD, FFT, and FFT-wd algorithms with respect to several parameters of the imaging process. To improve the readability of the image data, a pre-imaging process was also carried out using a contrast-limited adaptive histogram equalization in the *PIVlab*. All the algorithms were implemented with the same overlap of 50%. Based on a study of the accuracy evaluation performed by Thielicke (2014), the size of the interrogation window during every pass was set to the same value in the case of using the FFT-wd algorithm. In addition, the spline interpolation was used when the interrogation window was deformed between two passes.

To quantitatively evaluate the accuracy of these algorithms, analyses of the bias error ( $\epsilon_{\text{bias}}$ ) and random error ( $\epsilon_{\text{rms}}$ ) were introduced. Both the errors contribute to total error of a measurement system (Menditto et al. 2007; Thielicke 2014). The bias error determines trueness of the estimated values. Trueness is defined

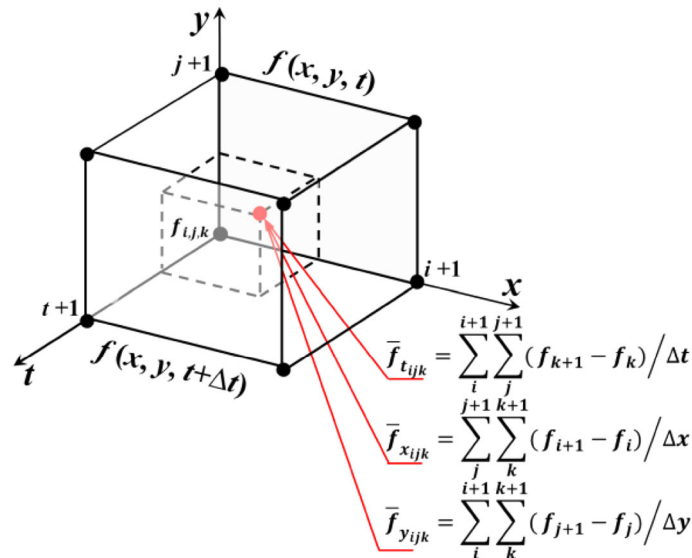


Fig. 2 A cube formed by eight brightness values from undistorted and distorted image

**Table 1** Comparisons of algorithms under parameters of imaging process

Processing algorithm	STD	FFT	FFT window deformation
CLAHE, size (px)	25	25	25
Sub-pixel estimator	Gradient method	Gaussian 2 × 3-point	Gaussian 2 × 3-point
Overlap (%)	50	50	50
Pass 1 int. area (px)	4 × 4	4 × 4	4 × 4
Pass 2 int. area (px)			4 × 4
Pass 3 int. area (px)			4 × 4
Pass 4 int. area (px)			4 × 4

as the agreement between the mean value and true value. The random error determines precision of the estimated values. Precision is a measure of the spread of the estimated values. The bias error is calculated as follows:

$$\varepsilon_{\text{bias}} = \frac{1}{m} \sum_{i=1}^m d_{\text{meas},i} - d, \quad (5)$$

where  $d_{\text{meas},i}$  is the displacement estimated by the above-mentioned algorithms,  $d$  is the true value, and  $m$  is the number of the displacements used in the analysis. In the present study, the true value,  $d$ , is used to evaluate the accuracy on the estimation in the regions where the displacements are not affected by an underwater shock wave, i.e.,  $d = 0$  in this regions.

The random error is determined as

$$\varepsilon_{\text{rms}} = \sqrt{\frac{1}{m} \sum_{i=1}^m (\overline{d_{\text{mean}}} - d_{\text{meas},i})^2}, \quad (6)$$

where  $\overline{d_{\text{mean}}}$  is the mean value calculated from the estimated displacements when  $i$  is from 1 to  $m$ .

#### 4 Reconstruction

Based on Eqs. (1) and (2), the Poisson equation is presented as follows:

$$\frac{\partial^2 N}{\partial x^2} + \frac{\partial^2 N}{\partial y^2} = \frac{Z_B}{Z_{Df}} n_0 \left( \frac{\partial \Delta x}{\partial x} + \frac{\partial \Delta y}{\partial y} \right), \quad (7)$$

where  $N$  is expressed as the integration of the refractive index difference along the optical path as shown in Eq. (8)

$$N = \int_{Z_D - \Delta Z_D}^{Z_D + \Delta Z_D} [n(x, y, z) - n_0] dz. \quad (8)$$

In this study, the center differential method was applied to the solving of Eq. (7).

Next, the FBP algorithm with a Shepp–Logan filter, as used by Venkatakrishnan and Meier (2004), was introduced to reconstruct the projections obtained from the Poisson equation. The radial distribution of the pressure was obtained from the Lorentz–Lorenz equation Eq. (9) and the Tait equation Eq. (10).

$$\frac{(n^2 - 1)}{\rho(n^2 + 2)} = \text{constant}, \quad (9)$$

$$P = (P_0 + B) \left( \frac{\rho}{\rho_0} \right)^\gamma - B, \quad (10)$$

where  $P$  is the pressure,  $\rho$  is the density.  $B = 2963$  bar,  $\gamma = 7.415$ , and  $P_0 = 1.013$  bar.

## 5 Results and discussions

Figure 3 shows the sequential BOS observation of the first shock wave generated by the expansion of the thermal plasma using the high-voltage–power supply shown in Fig. 1. The resolution was  $320 \times 64$  pixels, the frame rate was 300 kfps, and the exposure time was 200 ns. A reference image of the dot-pattern background, as shown in Fig. 3, shows that a dot with a diameter of  $720 \mu\text{m}$  covers about four pixels, so that the spatial resolution of the obtained image is  $180 \mu\text{m}$  per pixel. Therefore, the focal distance  $f$  in Eq. (7) is calculated to be about 160 mm through the principle of optics. From the phenomena shown in Fig. 3, it is found that the underwater shock wave indeed gives rise to the deformation of the dots in the background beside the displacements. The propagations of the first shock wave are observed through the distortion of the dots in Fig. 3(1)–(5). Subsequently, to evaluate the accuracy of the algorithms, the background-element displacements in Fig. 3(2) were estimated using the FFT, FFT-wd, and STD algorithms for interrogation windows of different sizes. In the analysis, it is assumed that the structure of a shock wave generated by underwater electric discharge is point-symmetric. Hence, the vectors of the background-element displacements in each interrogation window were decomposed as the radial and tangential components. The radial components of the displacements were used in the following analysis of the accuracy.

Figure 4 compares the background-element displacements obtained using different algorithms for interrogation windows of different sizes. The abscissa is the radial distance from the discharge point and the ordinate is the radial components of the displacements. In Fig. 4, the region from the discharge point to 50 pixels is affected by the discharge flush. The distorted region induced by the underwater shock wave is from 50 pixels to 120 pixels and the undistorted region is from 120 pixels. The open circles, squares, and triangles represent the displacements obtained with the STD, FFT, and FFT-wd algorithms, respectively. Generally speaking, all three algorithms can successfully estimate peak values of the displacements for every size interrogation window despite the estimated displacements being not the same. However, the FFT algorithm does not produce a clear peak for the  $4 \times 4$ -pixel window. It is also found that the peak values in the negative direction at a position of about 110 pixels disappear gradually as the size of the interrogation window increases. The reason for this is that the displacements within an interrogation window are assumed to be constant, therefore, a large size interrogation window causes a loss of the information due to the small compressibility of water. This suggests that an interrogation window of less than  $8 \times 8$  pixels should be used to prevent a loss of the information. Next, for every size interrogation window, the peak values of the displacements and the corresponding positions obtained with different algorithms were extracted to quantitatively analyze the accuracy of the algorithms in the distorted region. Furthermore, the bias error and the

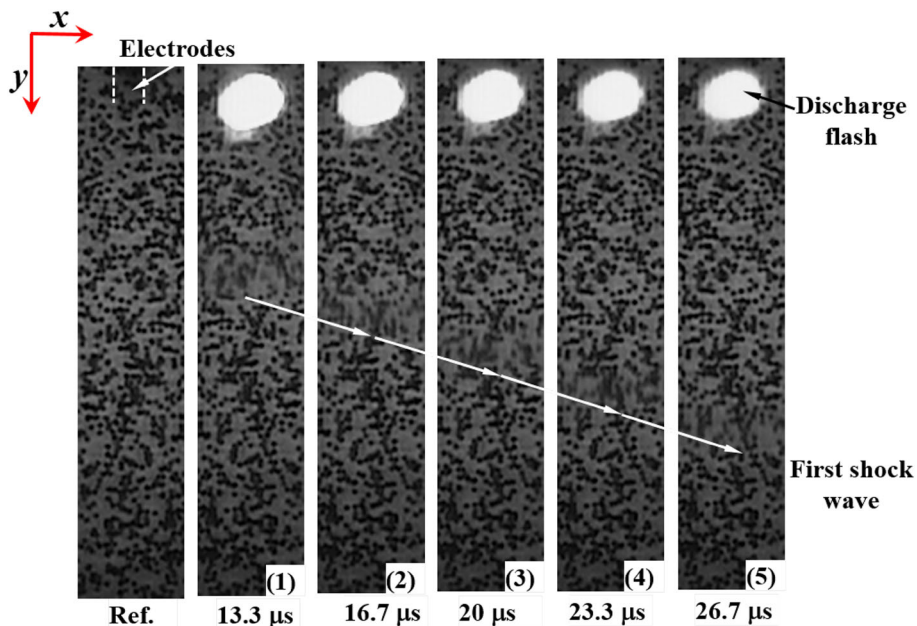
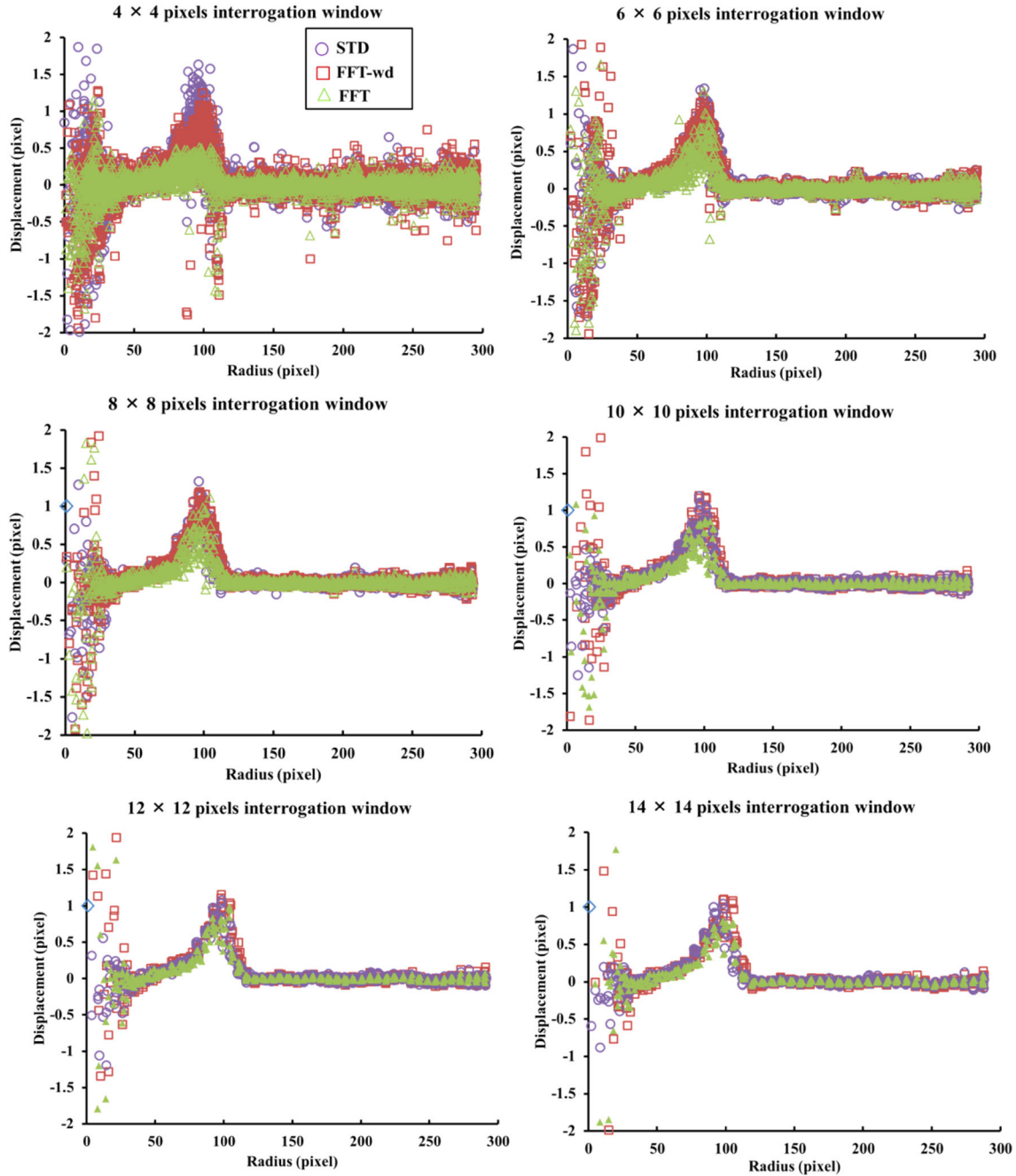


Fig. 3 Sequential observation of first shock wave generated by electric plasma expansion in BOS system



random error were performed to evaluate the trueness and precision of the estimated displacements in the undistorted region, respectively.

Figure 5a and b shows the peak values of the estimated displacements and the corresponding positions obtained with different algorithms for interrogation windows of different sizes. The abscissa  $L_{\text{pix}}$  is the pixel count for one side in length of the square interrogation window. Solid circles, squares, and triangles on curves represent the results obtained with the STD, FFT-wd, and FFT algorithms, respectively. In Fig. 5a, for the STD algorithm, the peak value of the displacements obtained for  $L_{\text{pix}} = 4$  is high compared with the values obtained for windows of other sizes. However, the STD algorithm provides a relatively similar estimate to that of the FFT-wd at  $L_{\text{pix}} = 6$  and larger. The FFT-wd algorithm detects almost constant peak



**Fig. 4** Comparisons of displacements estimated using different algorithms for interrogation windows of different sizes:  $\circ$  STD algorithm,  $\square$  FFT-wd algorithm, and  $\triangle$  FFT algorithm

values while the largest fluctuations are observed when using the FFT algorithm. In Fig. 5b, the standard deviations are calculated to 1.029 for STD, 1.819 for FFT-wd, and 3.209 for FFT algorithm. According to the standard deviations, the STD algorithm produces the smallest fluctuations on the corresponding positions of the peak values. For windows of a size exceeding  $L_{\text{pix}} = 8$ , the STD and the FFT-wd algorithms provide almost identical same results. On the other hand, the STD and FFT algorithms share the same values for windows smaller than  $L_{\text{pix}} = 6$ . Considering the steady estimates of the peak values and the corresponding positions, the STD algorithm with a window larger than  $6 \times 6$  pixels and the FFT-wd algorithm with a window larger than  $8 \times 8$  pixels can accurately detect the background-element displacements in the distorted region. However, as shown in Fig. 4, the large size of the window induces the information loss. Furthermore, a disadvantage of the FFT-wd algorithm is high cost of computation relative to the STD algorithm, especially for small interrogation windows.

Figure 6 shows the evaluation of the accuracy of the estimated displacements in the undistorted region using different algorithms for interrogation windows of different sizes. The bias errors and random errors were calculated using Eqs. (5) and (6). In the undistorted region, the true displacement  $d$  was 0 in Eq. (5). In Fig. 6a, the dashed lines represent the averages of the bias errors obtained with the three algorithms. The FFT-wd algorithm almost produces the largest bias errors from  $L_{\text{pix}} = 4$  to 14. Although the STD and the FFT algorithms provide a similar level of the results, the former shows the smallest bias errors for an interrogation window smaller than  $L_{\text{pix}} = 6$ . It is suggested that the STD algorithm produces a more accurate estimate of the displacements in the undistorted region. As shown in Fig. 6b, the random errors decrease remarkably for all the curves when  $L_{\text{pix}} = 4$  to 6. Consequently, to ensure a small random error, it is better to use an interrogation window larger than  $L_{\text{pix}} = 6$ . The FFT algorithm presents the smallest random errors for every size interrogation windows while the FFT-wd algorithm produces almost the largest errors. As a result, the STD and FFT algorithms provide a higher level of the accuracy in the undistorted region. However, the FFT algorithm performs badly when used to analyze the peak values and corresponding positions as shown in Fig. 5. Consequently, based on the results shown in Figs. 5 and 6, it is suggested that the STD algorithm, when used with a small window, provides a more accurate background-element displacement from the perspective of integrity of information, steady estimates of peak value, corresponding position in the distorted region, trueness and precision of the displacements in the undistorted region, high spatial resolution, and low computational cost.

Given the above-mentioned considerations, the STD algorithm with an interrogation window of  $6 \times 6$  pixels is used to estimate the background-element displacements of the images in Fig. 4. Figure 7 shows the vector distributions of the displacements induced by the first shock waves. The regions in the circles are affected by the discharge flush. From the vector fields, the propagation of the first shock wave is clearly distinguished. The vector covers about 60 pix, i.e., 10.8 mm. However, the width is suggested not to represent the width of the shock front since the flow behind the shock front also affects the dot deviation on the background. It can be seen that almost all of the vectors are pointing toward upstream except a small region where the vectors are in the direction of the shock wave propagation. According to the Eqs. (1) and (2), the displacement vectors are related to the density gradient  $\nabla\rho$ . The vector should point towards the

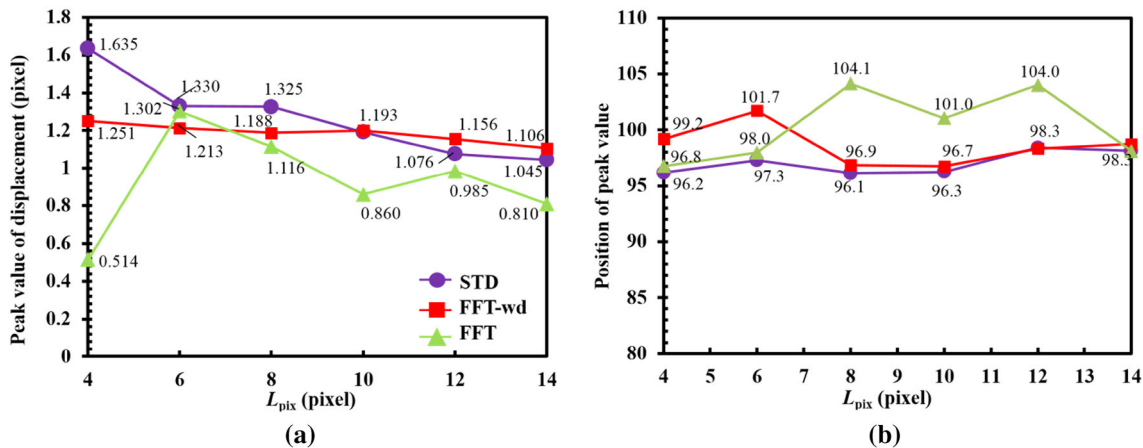
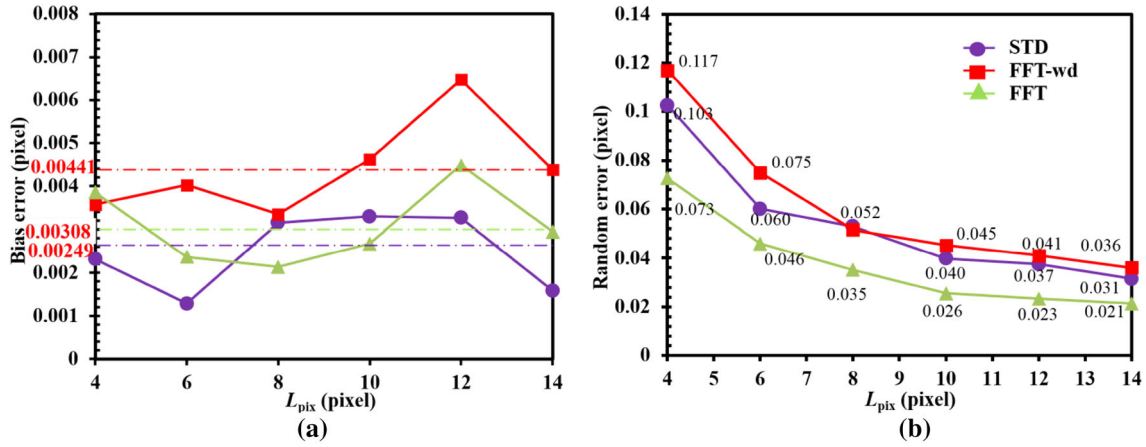


Fig. 5 Peak values of displacements **a** and corresponding positions **b** with variation in  $L_{\text{pix}}$





**Fig. 6** Evaluation of accuracy of displacements in undistorted region estimated using different algorithms for interrogation windows of different sizes: **a** Bias error and **b** Random error

propagation of a shock wave when it just arrives, i.e., the density changes from low to high value. When the density and pressure reach their peak across a shock wave front, the magnitude of the displacement increases. After that, the magnitude decreases and then increases in the opposite direction during the

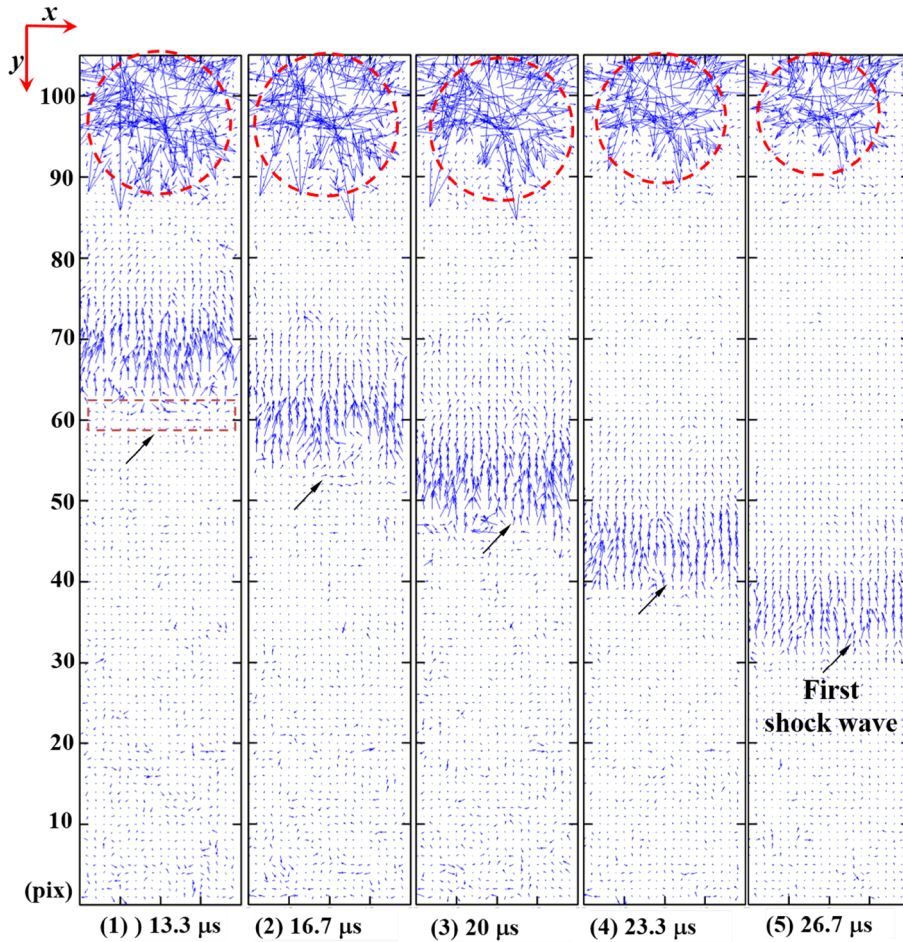


**Fig. 7** Vector distributions of background-element displacements obtained using STD algorithm with interrogation window measuring  $6 \times 6$  pixels

pressure going down behind the shock front. In the present paper, we obtained slightly different phenomena from what is described as mentioned above.

To investigate such distribution of the displacement vectors, the observation of first shock waves was carried out using the shadowgraph method as shown in Fig. 8. The frame rate of the high-speed camera (ULTRA Cam HS-106E, Nac Image Technology) was 300 kfps and the exposure time was 200 ns. In Fig. 8 (1), two electric discharge flashes are observed at the tips and base of the electrodes, so that multiple shock waves are generated at almost the same timing from different discharge points of the electrodes. Subsequently, the multiple shock waves, produced at slightly different positions, propagate outwards and the superposition of the shock waves occurs as shown in Figs. 8(2)–(4). Hence, the high-resolution analysis can identify the details of the flow with the interaction of the multiple shock waves, such that it is thought that the vectors point in different directions near the shock wave fronts for this reason. Because the density gradients are affected by the superposition of these multiple shock waves with different magnitudes and, therefore, the changes in the refractive index become complex. From the figure, it can be seen that the width of the shock waves is about 3.3 mm.

The background-element displacements shown in Fig. 7 were substituted into the Poisson equation to calculate,  $N$ , the projection of the refractive indices using the central differential method. Here,  $N = 0$  were used as the boundary conditions. Reminding that the structure of a first shock wave is assumed to be point-symmetric, which can be verified in Fig. 8. Hence, we obtained a circumferential average of the projection  $N$ . The projection number was about 98 from the discharge point to the far edge of the undistorted region in the radial distribution. Next, a projection field of  $196 \times 196$  was attained using these mean projections to determine values in other positions of the circumferential direction according to the circle structure. The projection field was reconstructed using the FBP algorithm with a Shepp–Logan filter, which is described in detail in the study of Venkatakrishnan and Meier (2004) and provided by MATLAB. Here, there was  $N = 0$  in the area around the discharge point to avoid the influence of the discharge flash on the reconstruction. The radial distribution of the refractive indices  $n$  was just used to acquire the pressure since no problem was thought not to be induced by the algorithms or the projection field in the reconstruction process.

Figure 9 shows the time variations in the pressure distributions of the first shock waves. The distances between the shock fronts are presented in the figure. The propagation speed of underwater shock wave is obtained to about 1474 m/s, which agrees with the theoretical value about 1500 m/s. In the figure, the shapes of the shock fronts are not steep and there is a small pressure increase in front of the main shock wave. To investigate the accuracy for estimating the magnitude and shape of the first shock wave, an experimental measurement was carried out using Fiber Optic Probe Hydrophone (FOPH 2000), as shown in Fig. 10. The FOPH pressure transducer is able to detect the pressure signal via the changing light reflection at the fiber–water interface caused by the density influence on the refractive index of water. Hence, it measures successfully pressure regardless of the electric noise, but slightly affected by the discharge flash. Figure 10 shows the experimental profile of first shock wave. For a comparison between the BOS and experimental results, it is found that the pressure profile estimated by BOS is similar to the experimental profile. In Fig. 10, the first two shock waves (FSW1 and FSW2) are clearly recorded within the time difference of  $0.7 \mu\text{s}$ . In addition, the pressure rise of the FSW1 shows increasing in steps, such that some shock waves are put all together in front of the FSW1. Consequently, the superposition of shock waves shown in Fig. 8 is thought to be a main reason for the appearance of such shapes on the shock fronts. Furthermore, based on the experimental profile, the expansion region behind the FSW1 is found, and it is confirmed that similar expansion regions are also obtained in the BOS estimates in Fig. 9. The peak pressure value at 20 mm from the discharge point in Fig. 9 shows good agreements with the experimental result in

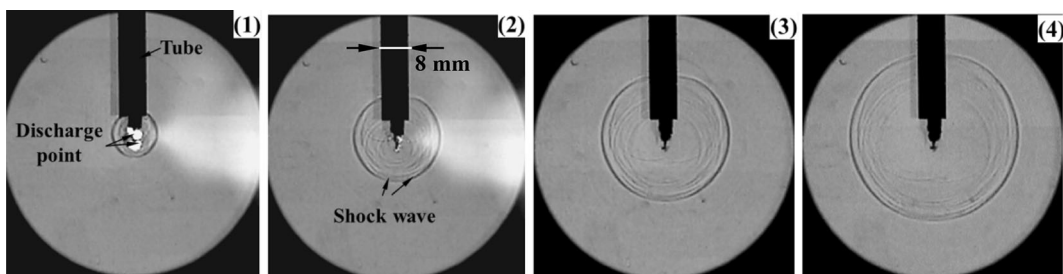


Fig. 8 Sequential observation of first shock waves using shadowgraph method

Fig. 10. However, the pressures within the expansion regions are quantitatively different in the two cases. The reason is assumed that the Tait equation was used during the reconstruction process in the BOS analysis. Remind that the FSW 2 in the experimental profile is not found in the BOS estimates. This is because the pressure measurements and the BOS observations were not synchronized.

The peak pressures of the first shock wave shown in Fig. 9 are represented together with the experimental data in Fig. 11. Solid squares on curves with error bars are of averages value for 10-time experimental measurements obtained with the FOPH pressure transducer. The top and bottom of the error bar shows the maximum and minimum among these measurements, respectively. The pressures estimated using the BOS technique, indicated by the solid triangles, gradually decrease from 20.65 MPa at 19.98 mm to 8.63 MPa at 37.26 mm. The error bar presents the uncertainty in the experimental measurements. The pressure values in the ranges of the error bars are suggested to be reasonable. Hence, the estimated pressures are in good agreements with the experimental data. As a result, the qualitative estimation with the present BOS technique is thought to be reasonable. Next, the BOS technique was used to measure the pressures of the rebound shock waves generated by the collapse of a vapor bubble at the tip of the electrodes.

Figure 12 shows the sequential BOS observations of the rebound shock waves generated by the collapse of a vapor bubble. The high-speed camera captured images under the same conditions as that in Fig. 3. A vapor bubble generated by the electric discharge at the tips of the electrodes grew to a maximum diameter of about 8 mm. In Fig. 12(1), the generation of a rebound shock wave (RSW1) is observed from the distortion of the dots. Another shock wave is also captured in Fig. 12(3). This could be a second rebound shock wave (RSW2) or a reflected shock wave at the tube of the electrodes. To distinguish rebound shock wave from reflected shock wave, an experiment based on the shadowgraph method were carried out under the same conditions as that in Fig. 8. The images are showed in Fig. 13. Based on the shadowgraph observation, the shock wave in Fig. 12(3) is distinguished as RSW2. The vapor bubble at the tips of the electrodes cannot remain spherical during the collapse, such that several rebound shock waves are generated at different timings. As shown in Figs. 13(1) and (2), a precursor wave is also captured before RSW1 and RSW2. These waves are also considered to be almost from the same position.

Figure 14 shows the vector distributions of the background-element displacements induced by the rebound shock waves. From the vector fields, the generation and propagation of RSW1 and RSW2 can be clearly observed. The directions of the vectors are toward the propagation of the rebound shock wave.

Figure 15 shows the time variations of the pressure distributions estimated using the BOS technique in the case of the rebound shock waves. In the pressure waveforms, these regions of the negative pressures before the rebound shock wave (RW1) front are found, but the regions are not found in the case of the first shock waves in Fig. 10. Therefore, the cause of the phenomena is not thought to be related to the algorithms used in the present BOS system. Here, two main reasons are considered. First, the planar-reflected shock

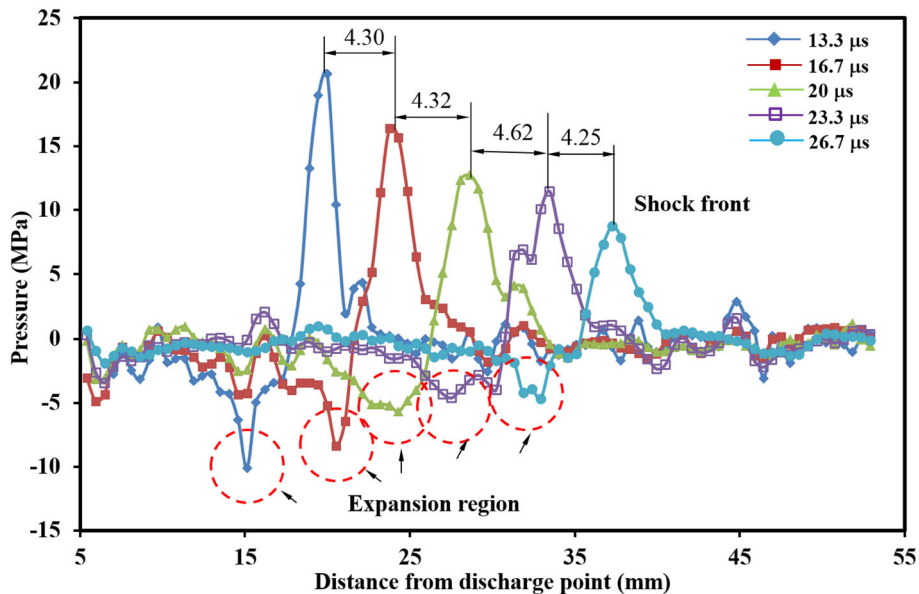


Fig. 9 Pressure distributions of first shock wave estimated with BOS technique at different times

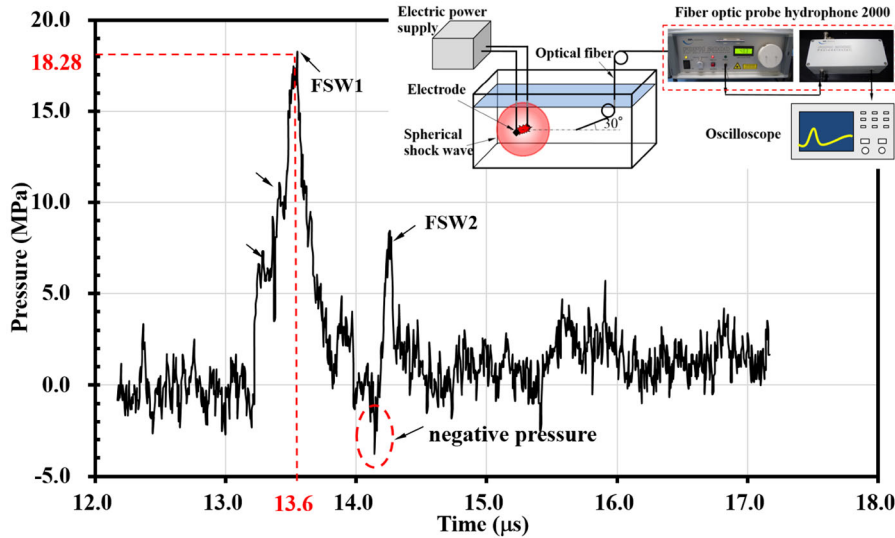


Fig. 10 Pressure profile of first shock waves measured 20 mm from discharge point using FOPH pressure transducer

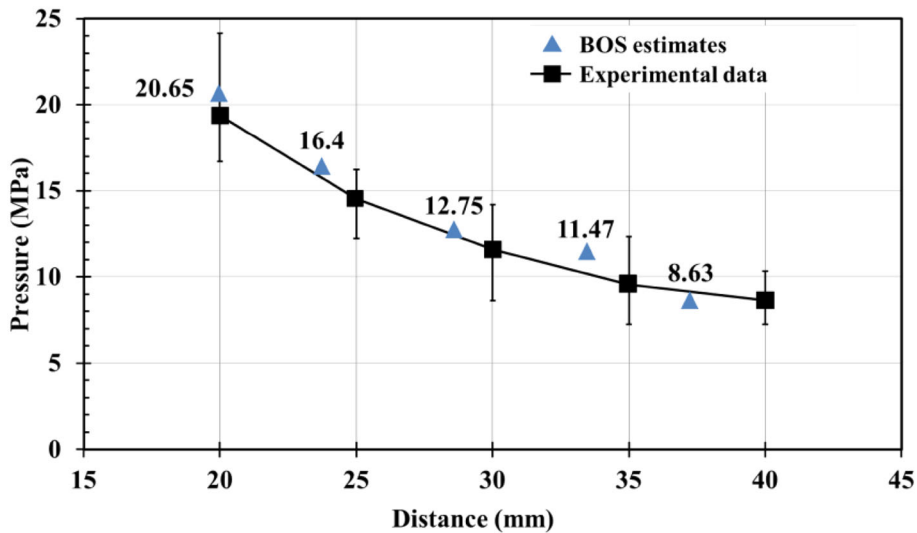
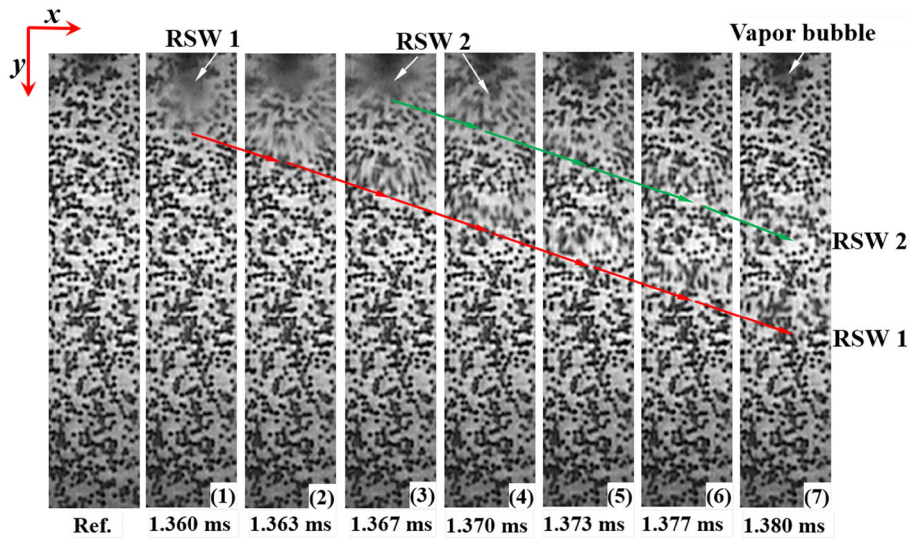


Fig. 11 Comparison of pressure attenuation behind first shock wave, as determined by experimental measurements and BOS estimates

waves shown in Fig. 13 affect the pressure field in the region before the rebound shock wave is generated. The second reason relates to the motion of the vapor bubble. After the first shock wave is generated, a vapor bubble is induced at the tips of the electrodes. The bubble expands to its maximum size and, then immediately and quickly contracts, such that the water around the bubble is stretched by its contraction motion and tensile stress is generated, giving rise to a region of negative pressure. Next, the surface of the vapor bubble re-expands from the minimum radius and compresses the water around the bubble at an extremely high velocity. The rebound shock wave is generated at the beginning of the re-expansion motion. At this time, the water around the bubble is forcefully compressed by the shock front. However, the re-expansion velocity at the bubble surface is much slower than that of the rebound shock wave, so that the water behind the rebound shock wave is also acted on by the tensile stress. Therefore, an expansion region also occurs behind the rebound shock front, as shown in the BOS estimates of Fig. 15. In experimental pressure measurements, the expansion regions in front of and behind the rebound shock front were obtained as shown in Fig. 16. Consequently, from the perspective of the features on the pressure waveform, the BOS estimates maintain their consistency with the experimental results.





**Fig. 12** Sequential observation of rebound shock wave generated by collapse of vapor bubble in BOS system

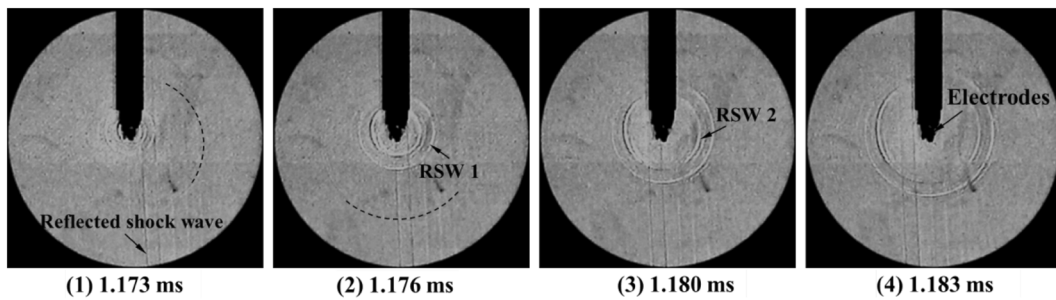


**Fig. 13** Observation of rebound shock waves using shadowgraph method

The peak pressures of the RSW1 and RSW2 in Fig. 15 are presented together with the experimental data in Fig. 17. Solid diamonds on curves indicate the experimental measurements obtained using the FOPH pressure transducer. In fact, the collapse of the vapor bubble induced by the underwater electric discharge was not controlled, and thus the number and pressure values of the generated rebound shock wave were scattered. To obtain accurate pressure attenuation, the pressures were measured in the experiments when only one rebound shock wave was generated. The pressure behind the rebound shock wave decreases from 60.6 MPa at 6 mm to 13.9 MPa at 30 mm, relative to the center of the vapor bubble. Solid squares and triangles on curves indicate the peak pressures of the RSW1 and RSW2, respectively. The pressure behind the RSW1 decreases from 50.52 MP to 13.85 MPa while that for RSW2 decreases from 24.12 to 13.34 MPa. By comparing the BOS estimates with the experimental data, the pressures behind the two rebound shock waves can be seen to be smaller than that when only one shock wave is generated. This phenomenon in this figure is thought to be reasonable and hence the pressures estimated by the BOS technique are in good agreement with the experimental data. On the other hand, the pressures were not obtained within a region of less than 6 mm when using the pressure transducer. This is because that the bubble surface impacts the pressure transducer during the expansion motion so that the measurement is seriously disturbed. However, the BOS technique can quantify the pressures in the region only using images. Moreover, it is also difficult to set several pressure transducers around smaller bubbles to obtain pressure attenuation behind a rebound shock wave. Consequently, it is expected that the BOS technique will probably overcome the problem associated with conventional pressure measurement related to the collapse of microbubbles, and become a promising means of quantitatively measuring high-speed phenomena.



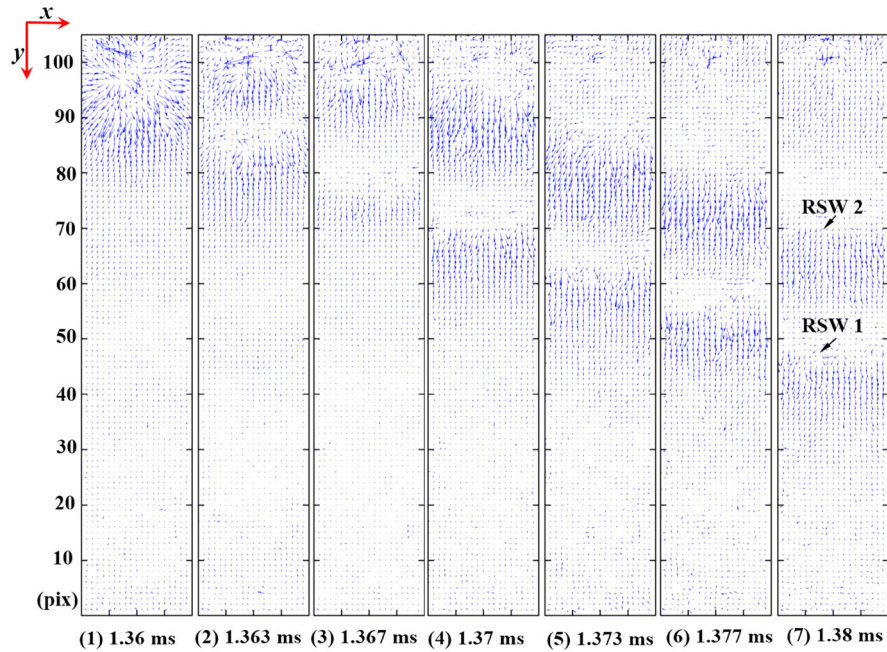


**Fig. 14** Vector distributions of displacement obtained using STD algorithm with interrogation window measuring  $6 \times 6$  pixels

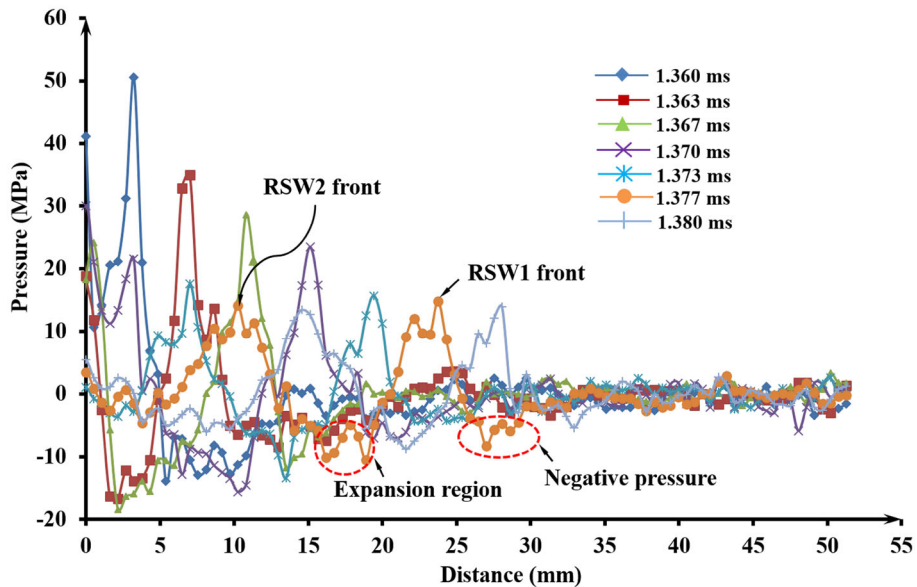


**Fig. 15** Time variations of pressure distributions of rebound shock waves estimated using BOS technique

## 6 Conclusion

This paper attempted to measure the pressures of the rebound shock waves generated by the collapse of a vapor bubble, using the BOS technique. The vapor bubble was generated by an underwater electric discharge at the electrodes. In the imaging process, we used the STD algorithm to detect the background-element displacements induced by the underwater shock wave. By comparing the accuracy of the STD, FFT and FFT-wd algorithms, the STD algorithm was suggested as a mean of accurately estimating sub-pixel

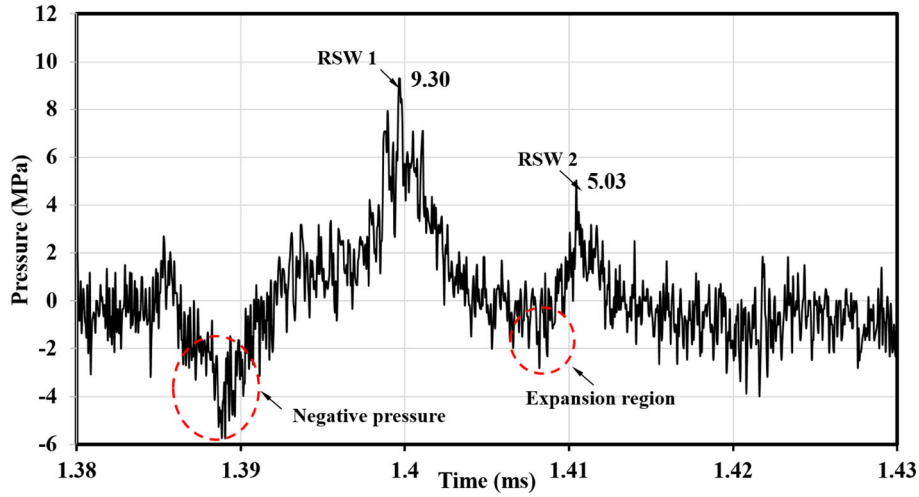


Fig. 16 Pressure profile of rebound shock waves measured 30 mm from discharge point using FOPH pressure transducer

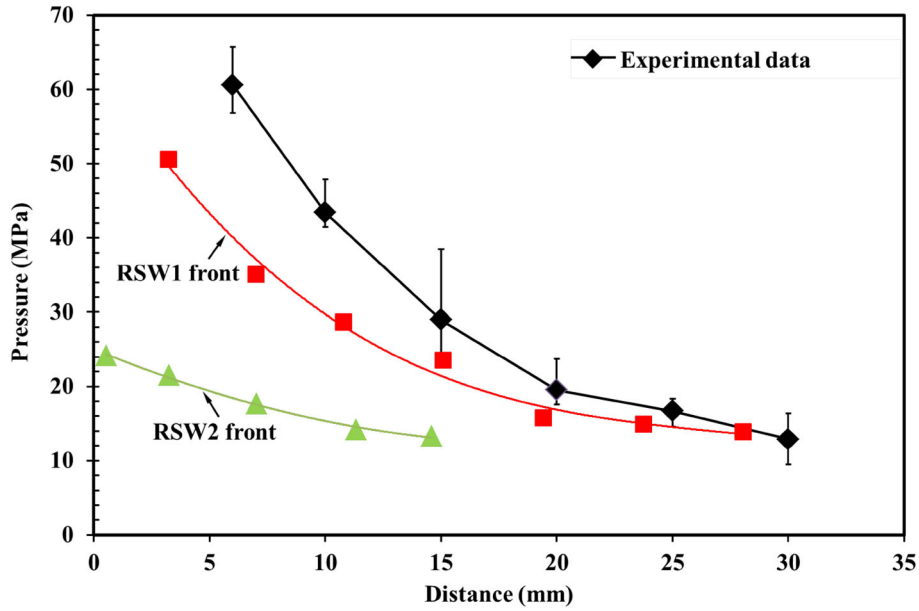


Fig. 17 Pressure attenuations of rebound shock wave generated by collapse of vapor bubble: ■ RSW1 obtained with BOS technique, ▲ RSW 2 obtained with BOS technique, and ◆ experimental measurement using FOPH 2000

displacements from a pair of images. Next, the FBP algorithm with a Shepp–Logan filter was used to reconstruct the projections obtained with the Poisson equation on a basis of these estimated displacements. The radial distributions of the pressures were obtained using the Lorentz–Lorenz equation and the Tait equation. As a result, the shapes of the shock fronts estimated by the BOS technique were not steep and expansion regions were found behind the shock fronts in the pressure waveforms. However, similar pressure profiles were also observed in the experimental measurements. From the shadowgraph observations, it was found that the superposition of the shock waves occurred because many shock waves were generated at different positions of the electrodes and different timings with the trigger of the electric discharge. Moreover, the pressure attenuation behind the first shock wave, as estimated by BOS technique, was in good agreements with the experimental measurements. For the rebound shock waves generated by the collapse of a vapor bubble, the non-spherical collapse led to the generation of several strong shock waves. The pressure attenuations behind the RSW1 and RSW2 estimated by the BOS technique proved to be reasonable compared to the experimental data. It is concluded that the present BOS technique is capable of measuring the

pressure of an underwater shock wave quantitatively and precisely, and even is a promising mean of qualifying the collapse of microbubble.

**Acknowledgements** A part of this work was supported by JSPS KAKENHI Grant Number 16H04600 and 16K14512, National Natural Science Foundation of China through grant numbers 11772340 and 11332011. In addition, we would like to sincerely thank Nac Image Technology Inc. for the supply of optical experimental equipment.

## References

- Hayasaka K, Tagawa Y, Liu T, Kameda M (2016) Optical-flow-based background-oriented schlieren technique for measuring a laser-induced underwater shock wave. *Exp Fluids* 7(12):179
- Horn BK, Schunck BG (1981) Determining optical flow. *Artif Intell* 17(1–3):185–203
- Kindler K, Goldhahn E, Leopold F, Raffel M (2007) Recent developments in background oriented schlieren methods for rotor blade tip vortex measurements. *Exp Fluids* 43(2–3):233–240
- Liu T, Shen L (2008) Fluid flow and optical flow. *J Fluid Mech* 614:253–291
- Meier GEA (1999) Hintergrund-Schlierenverfahren. Patent pending, Deutsches Patentamt
- Meier GEA (2002) Computerized background-oriented schlieren. *Exp Fluids* 33(1):181–187
- Menditto A, Patriarca M, Magnusson B (2007) Understanding the meaning of accuracy, trueness and precision. *Accred Qual Assur* 12(1):45–47
- Nishio S, Okuno T (1998) Statistical approach to the measurement of velocity field. *J Vis* 1(2):161–170
- Okuno T (1995) Image measurement by means of spatio-temporal derivative method. In: *Proceeding of the International Workshop on Particle Imaging Velocimetry, Japan*
- Raffel M, Tung C, Richard H, Yu Y, Meier G E A (2000) Background oriented stereoscopic schlieren (BOSS) for full scale helicopter vortex characterization. In: *Processing of 9th International Symposium on FlowVisualization, Scotland*
- Richard H, Raffel M (2001) Principle and applications of the background oriented schlieren (BOS) method. *Meas Sci Technol* 12(9):1576
- Sugii Y, Nishio S, Okuno T, Okamoto K (2000) A highly accurate iterative PIV technique using a gradient method. *Meas Sci Technol* 11(12):1666–1673
- Thielicke W (2014) *The Flapping Flight of Birds—Analysis and Application*. Dissertation, University of Groningen
- Venkatakrishnan L, Meier G (2004) Density measurements using the background oriented schlieren technique. *Exp Fluids* 37(2):237–247
- Venkatakrishnan L, Suriyanarayanan P (2009) Density field of supersonic separated flow past an afterbody nozzle using tomographic reconstruction of BOS data. *Exp Fluids* 47(3):463–473
- Venkatakrishnan L, Surigyanaraynan P, Jagadeesh G (2013) Density field visualization of a micro-explosion using background oriented schlieren. *J Vis* 16(3):177–180
- Yamamoto S, Tagawa Y, Kameda M (2015) Application of background-oriented schlieren (BOS) technique to a laser-induced underwater shock wave. *Exp Fluids* 56(5):1–7